MATERIALS SCIENCE

An imidazolium-based zwitterionic polymer for antiviral and antibacterial dual functional coatings

Pengyu Chen, Jiayan Lang, Yilun Zhou, Alexandra Khlyustova, Zheyuan Zhang, Xiaojing Ma, Sophie Liu, Yifan Cheng, Rong Yang*

To reduce the severe health risk and the huge economic impact associated with the fomite transmission of SARS-CoV-2, an imidazolium-based zwitterionic polymer was designed, synthesized, and demonstrated to achieve contact deactivation of a human coronavirus under dry ambient conditions that resemble fomite transmission. The zwitterionic polymer further demonstrated excellent antifouling properties, reducing the adhesion of coronavirus and the formation of bacteria biofilms under wetted conditions. The polymer was synthesized using a substrate-independent and solvent-free process, leveraging an all-dry technique named initiated chemical vapor deposition (iCVD). The broad applicability of this approach was demonstrated by applying the polymer to a range of substrates that are curved and/or with high-aspect-ratio nano/microporous structures, which remained intact after the coating process. The zwitterionic polymer and the synthesis approach reported here present an effective solution to mitigate viral transmission without the need for manual disinfection, reducing the health and economic impact of the ongoing pandemic.

INTRODUCTION

The ongoing pandemic outbreak due to coronavirus disease of 2019 (COVID-19), one of the most dangerous pandemics in human history, has caused millions of deaths and transformed the way of life. Fomite transmission, i.e., the transmission of severe acute respiratory syndrome coronavirus 2 (SARS-CoV-2) via contaminated surfaces (*1*), namely, fomite surfaces, has been considered a cause for community spread (*2*), which in turn caused a huge economic impact (*3*). By the end of 2020, global sales of surface disinfectant amounted to $4.5 billion, with the New York Metropolitan Transit Authority alone spending $484 million on COVID-19 response. The emerging variants of SARS-CoV-2 that are highly lethal and transmittable suggest that the virus will likely become a lasting threat to the public health (*4*), calling for materials that can resist the adhesion of viruses or deactivate them for the long-term health and economic benefits.

A critical challenge that limited the development of a long-term solution to fomite transmission is the ubiquity of potential fomites (*5*). Any surface, ranging from that of medical instruments to public facilities, and from industrial equipment to personal electronics, used under dry ambient conditions or in a wetted state (e.g., the conveyer belt in food processing facilities), can become a fomite (*6*). That ubiquity requires that antiviral materials must be applied in a substrate-independent and conformal manner (e.g., onto plastic wares, fabrics, and porous membranes) and that they remain effective under ambient or wetted conditions.

Furthermore, few studies to date have reported coatings with antiviral efficacy against coronaviruses. While a number of materials have been found to inactivate viruses upon contact [e.g., metal and inorganic materials based on their toxicity and/or ability to generate reactive oxygen species (*7*–*9*), polyelectrolytes (*10*, *11*), and photosensitizers (*12*, *13*)], their antiviral efficacy was often proven using influenza A virus or bacteriophages, which bear little resemblance to the SARS-CoV-2 (*14*). As a result, their reported antiviral efficacies may not be extrapolated to SARS-CoV-2 due to the unique architecture of coronaviruses (*6*). The emerging nanomaterials (e.g., Cu alloy and nanoparticles of metal oxide) that demonstrated deactivation of coronavirus often require incubation of the viruses with the materials to achieve the antiviral effect, a prerequisite that is challenging to meet in most scenarios to stop fomite-mediated transmission (*6*).

Hence, the long-term solution needed to reduce fomite transmission requires an antiviral material that (i) could be applied in a substrate-independent and conformal manner, (ii) demonstrates efficacy against coronaviruses, (iii) deactivates viruses without the need for incubation with medium [e.g., by demonstrating deactivation of viruses in aerosols (*12*), a main medium for fomite-mediated disease spreading (*5*)], and (iv) remains effective under dry ambient or wetted conditions. To meet these criteria, we designed an imidazolium-based zwitterionic polymer and demonstrated its anti-coronavirus characteristics in the context of (i) contact deactivation under dry ambient conditions and (ii) adhesion repelling under wetted conditions. The substrate-dependent and conformal synthesis and application of the imidazolium-based zwitterionic polymer was enabled by an all-dry technique, namely, initiated chemical vapor deposition (iCVD).

We chose to design a zwitterionic polymer based on the well-characterized antifouling properties of zwitterionic materials, which originate from its strong electrostatic interaction with water molecules (*15*, *16*). Recent research has further highlighted a variety of molecular interactions between the zwitterionic structures and aromatic-rich amino acids, such as Phe, Tyr, and Trp (*17*, *18*), through cation-π interactions or polar interactions (*19*), leading to the denaturation of proteins (e.g., the spike glycoprotein lining the surface of SARS-CoV-2) upon contacting zwitterionic moieties. The spike glycoprotein is a class I viral fusion protein, whose juxtamembrane domain is rich in aromatic amino acids and is highly conserved in all coronaviruses (*20*). Although zwitterionic materials have not been used to deactivate coronaviruses (*21*, *22*), we predicted that an imidazolium-based zwitterionic polymer has antiviral efficacy based on its distinct property that the carbon atom at the C2 position of imidazolium carries a considerable positive charge. Although the

Robert F. Smith School of Chemical and Biomolecular Engineering, Cornell University, Ithaca, NY 14853, USA.
*Corresponding author. Email: ryang@cornell.edu

imidazolium-based zwitterionic moiety has a net neutral charge, its electrostatic potential is distributed such that the carbon at the C2 position of the imidazolium ring carries a considerable positive charge, while the nitrogen and other nearby carbon atoms are slightly negatively charged. Hence, the hydrogen bonded to the C2 carbon in imidazolium has been reported to exhibit mild acidity, which makes it an excellent hydrogen bond donor, enabling enhanced interactions with amino acids.

The contact deactivation and adhesion repelling of coronaviruses achieved by the imidazolium-based zwitterionic polymer was demonstrated using a human coronavirus, HCoV-OC43. To demonstrate the broad-spectrum antifouling effect of the imidazolium-based zwitterionic polymer, we quantified *Pseudomonas aeruginosa* biofilm formation on imidazolium-based zwitterionic polymer surface, which was reduced to 15% of that formed on a polyvinylchoride (PVC) surface. Furthermore, imidazolium-based zwitterionic polymer reduced the production of a siderophore, namely, pyoverdine, in the biofilms to 33% of that on a PVC surface, implying that the biofilm on imidazolium-based zwitterionic polymer had lower pathogenicity (*23*).

To demonstrate the substrate-independent and conformal nature of the synthesis approach reported here, we applied the imidazolium-based zwitterionic polymer to a range of substrates, which are curved (i.e., microplates), or have complex three-dimensional (3D) microstructures (i.e., textiles), or have high-aspect-ratio nanopores (i.e., filtration membranes) (*24*). The imidazolium-based zwitterionic polymer is reproducible, substrate independent, and conformal over nano/microstructures. The versatility of the synthesis approach was enabled by iCVD, which deposits conformal and reproducible polymer coatings with precisely controlled thickness (*25*). Although an imidazolium-based zwitterionic polymer has not been synthesized using an all-dry technique previously, the scalability and robustness of the approach (*6*) promise its rapid progression along the discovery to deployment continuum of materials development, hence pointing to mitigated risk of virus spread and reduced economic penalty to control fomite transmission of COVID-19, enabled by the imidazolium-based zwitterionic polymer.

RESULTS

Synthesis of the precursor copolymers via iCVD

The imidazolium-based zwitterionic polymer was synthesized via a two-step vapor treatment (Fig. 1). In the first step, iCVD deposition of vinyl imidazole (VI; monomer) and divinylbenzene (DVB; cross-linker) was performed. The coating of copolymers was subsequently treated using a vapor of 1,3-propanesultone in a second step to obtain the imidazolium-based zwitterionic polymer (*26*, *27*).

The cross-linker, DVB, was included because the strong hydration of zwitterionic polymers often renders them soluble in aqueous environments. Introduction of DVB enabled durable coatings on a diverse range of substrates, which has been shown to reduce polymer solubility and enhance the mechanical strength of iCVD polymer coatings (*28*). The iCVD technique allows facile incorporation of cross-linkers due to its all-dry nature, using which films that are insoluble and ultradurable have been obtained (*25*).

Optimization of the composition of the copolymers

We systematically varied the composition of the copolymer films to simultaneously optimize (i) the antiviral/antibacterial performance, which calls for a greater VI content, and (ii) film durability, which calls for a greater DVB content (*29*). The copolymer composition was controlled by adjusting the flow rates of VI and DVB (Fig. 1), which in turn determined a key synthesis parameter, P^m/P^{sat}, i.e., the ratio of partial pressure of a monomer to its saturation pressure at the temperature of the stage. P^m/P^{sat} indicates the concentration of a monomer on the substrate surface (i.e., where the polymerization occurs) based on the Brunauer-Emmett-Teller isotherm (*30*). The sum of the P^m/P^{sat} values for VI and DVB was held constant at ~0.5 for all depositions to maintain a deposition rate of ~5 nm·min^{-1} and to prevent condensation of the monomers (which could cause defects in the film) (*31*). Furthermore, a patch flow of argon was used to keep the total gas flow rate constant, ensuring unchanged residence time inside the iCVD reactor during different deposition runs.

Successful polymerization of VI and DVB was confirmed, and composition of the copolymer films was quantified using x-ray photoelectron spectroscopy (XPS) and Fourier transform infrared spectroscopy (FTIR). An XPS survey scan confirmed the elementary composition of O, N, and C in the deposited polymer films (fig. S1, table S1). Note that appreciable oxygen concentrations were detected in the XPS survey scans, which were attributed to adventitious organic matters and the initiator radical, *tert*-butoxide. At the filament temperature used (i.e., 230°C), *tert*-butoxide is considered the dominating initiation species (*32*). Furthermore, the incorporation of oxygen from *tert*-butoxide was likely further enhanced because of its role as a terminating species given the low reactivity of VI. The FTIR spectra of poly(1-vinylimidazole) (PVI), poly(divinylbenzene) (PDVB), and copolymer films confirmed their chemical structure (Fig. 1C). The absorption band at 3105, 1512, and 664 cm^{-1}, attributed to the stretching vibration of C–H, C=N, and vibration of the imidazole ring, respectively, indicated the successful incorporation of VI into the polymer films (*33*). The adsorption of 2871 cm^{-1} came from unreacted vinyl bonds in the DVB, implying the presence of DVB units. The two peaks at 1228 and 1284 cm^{-1}, which are characteristic of the imidazole ring in VI, and the peak at 2871 cm^{-1} of DVB were used to calculate the content of VI unit in the copolymers because they do not overlap with other peaks and show strong adsorption.

Using the Beer-Lambert equation (*34*) and assuming that the bond oscillator strength is the same for all polymers synthesized here, the area under the peak for the double absorption at 1228 and 1284 cm^{-1} (imidazole ring) and that for the absorption at 2871 cm^{-1} (unreacted vinyl groups in DVB) were used to calculate the concentrations of VI and DVB, respectively, in the copolymers. A similar method has been reported previously for calculating the compositions of copolymers of DVB and 4-vinylpyridine (see Supplementary Materials for details) (*35*).

The results are summarized in Fig. 1B. The VI content in the copolymers ranged between 17 and 55% due to low reactivity of VI. The high degrees of cross-linking in these thin films are considered to improve the mechanical strength and thus durability, based on previous reports (*35*). The elemental compositions calculated using the XPS survey scans are shown in table S1, which demonstrated contents of VI that were slightly lower than those calculated using FTIR. We chose FTIR as the basis of our composition analyses due to the known sensitivity of XPS results to the dynamic surface chain reorientation (*36*) and contamination. The copolymers were named according to their VI compositions. For example, a

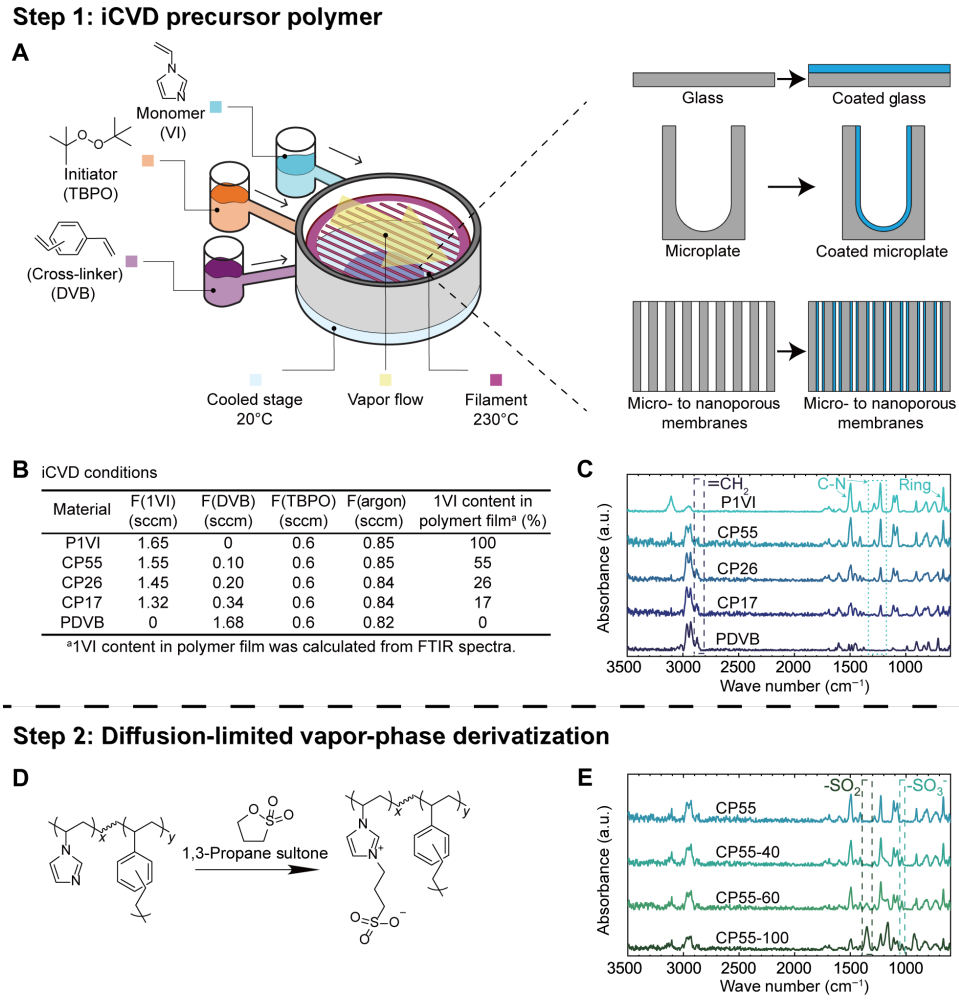

Material	F(1VI) (sccm)	F(DVB) (sccm)	F(TBPO) (sccm)	F(argon) (sccm)	1VI content in polymert film[a] (%)
P1VI	1.65	0	0.6	0.85	100
CP55	1.55	0.10	0.6	0.85	55
CP26	1.45	0.20	0.6	0.84	26
CP17	1.32	0.34	0.6	0.84	17
PDVB	0	1.68	0.6	0.82	0

[a]1VI content in polymer film was calculated from FTIR spectra.

Fig. 1. Synthesis of the imidazolium-based zwitterionic polymers and their chemical characterization using FTIR. (**A**) Scheme of the substrate-independent and conformal iCVD deposition. (**B**) Deposition conditions used in this report and the film compositions that resulted from those conditions. sccm, standard cubic centimeter per minute. (**C**) FTIR spectra of homopolymer of PVI; copolymers with the VI contents of ~55, ~26, and ~ 17%; and homopolymer of PDVB. The dashed rectangle indicates the characteristic peak of the methyl group in PDVB, and the dotted rectangle indicates the characteristic peaks of the C–N bond in the imidazole ring in PVI. (**D**) Derivatization reaction, where copolymer films were treated with 1,3-propanesultone for 24 hours. (**E**) FTIR spectra of copolymers treated with a vapor of 1,3-propanesultone at 40°, 60°, and 100°C, respectively. The dashed rectangles indicate the characteristic peaks of the SO_3^- symmetric vibration and the O=S=O asymmetric vibration. a.u., arbitrary units.

copolymer containing 55% VI and 45% DVB according to the FTIR-based calculation was labeled as "CP55" hereinafter.

Derivatization of the copolymers to obtain the zwitterionic moieties

The copolymer films were treated with a vapor of 1,3-propanesultone for 24 hours to convert the imidazole group to an imidazolium-based zwitterionic moiety. Temperature of that derivatization reaction was varied to strike a balance between high conversion rate, which is obtained at higher temperatures, and benign reaction conditions to ensure the applicability of this approach to a broad range of substrates, some of which may have limited thermostability. For example, the softening point (e.g., those determined by the heat deflection test) for common medical plastics, such as PVC or polystyrene, is ~70°C (*37*).

A series of derivatization reactions were performed on the copolymer obtained in step 1 with the greatest VI content, i.e., CP55, to maximize the achievable composition of zwitterionic moieties and thus antimicrobial efficacy. The derivatization temperatures of 40°, 60°, and 100°C were used, and 100°C was included as a control group where complete conversion was anticipated. To reflect the different derivatization temperatures, the treated copolymer samples were denoted with their VI content, followed by the derivatization temperature. For example, a copolymer containing 55% VI and 45% DVB and derivatized at 40°C was labeled as "CP55-40" hereinafter.

The successful obtainment of imidazolium-based zwitterionic polymer was confirmed using FTIR spectrum (Fig. 1E). The new peak at 1037 cm^{-1} was ascribed to the symmetric stretching of the SO_3^- group (Fig. 1D), indicating the formation of zwitterionic structure (*38*). To capture the concentration of the zwitterionic moieties in the whole film, the peak at 1352 cm^{-1}, characteristic of the anti-symmetric stretching of O=S=O, and the peak at 664 cm^{-1}, representing the unreacted imidazole ring, were compared. With the

increasing derivatization temperature, FTIR spectra of the treated samples presented a more pronounced peak at 1352 cm^{-1} and a diminishing peak at 664 cm^{-1}, indicating an increasing concentration of zwitterionic moieties in the polymer film (Fig. 1E and fig. S2). Nevertheless, as we demonstrated previously (*27*), the surface concentration of the zwitterionic groups is the most crucial for the antimicrobial efficacy of the polymer coatings, which was characterized in detail using high-resolution XPS.

Surface-concentrated zwitterionic moieties obtained by the all-dry synthesis approach

To investigate the surface concentrations of the imidazolium-based zwitterionic moieties in the derivatized films, XPS survey scan and high-resolution scans on the N(1s), C(1s), and S(2p) were performed (Fig. 2B and figs. S3 to S5). The peak at 401.5 eV corresponded to the N(1s) in the imidazolium ring (colored green in Fig. 2B), whereas the peaks at 399.5 and 400.6 eV corresponded to the two unreacted nitrogen atoms in PVI (colored orange and blue, respectively, in Fig. 2B) (*39*, *40*). While increasing the derivatization temperature from 40° to 60°C led to a mild increase in the conversion rate, from 51.5 to 70.2%, further increasing it to 100°C did not yield further increase in the rate of conversion (78.9%) (Fig. 2B). The C(1s) and S(2p) high-resolution scans further confirmed this composition of the film surfaces. The convoluted carbon signals shown in fig. S3 were attributed to the three classes of chemical environments (i.e., the carbon between the two nitrogen atoms in the imidazole ring, the carbon next to the nitrogen or sulfur, or the carbon surrounded by carbon), the compositions of which were consistent with the results from the N(1s) scans. The S(2p) high-resolution scan confirmed the SO_3^- moiety. Hence, the derivatization temperature of 60°C was chosen for subsequent experiments due to the high rate of conversion achieved at this temperature while remaining below the common softening point discussed above.

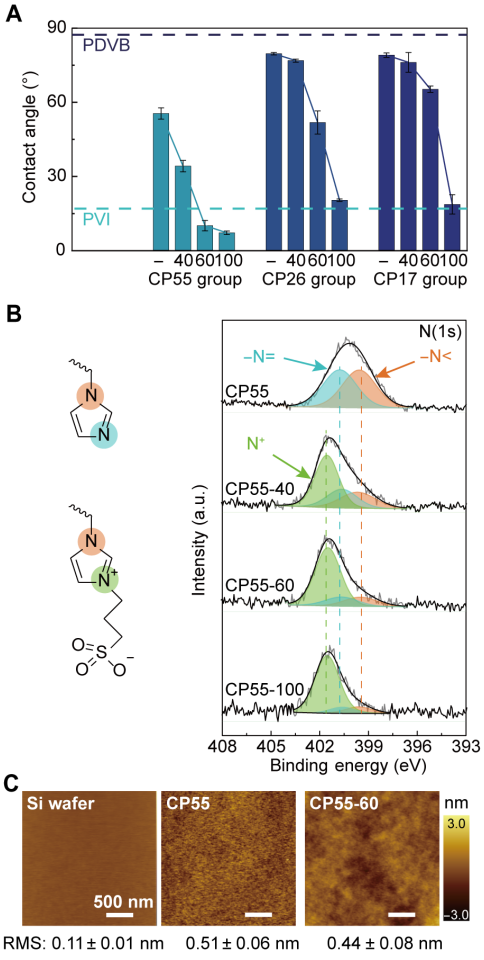

Fig. 2. Characterization of the material surface properties using CA, high-resolution XPS, and AFM. (**A**) CA on the as-deposited and derivatized copolymers, i.e., CP55, CP26, and CP17, where CA for each film was measured at the derivatization temperatures of 40, 60, and 100°C. The dashed lines indicated the CA values of PVI and PDVB, respectively. (**B**) Chemical structures of imidazole and the imidazolium-based zwitterionic moieties and their XPS high-resolution scans of N(1s) for CP55 and its derivatives. (**C**) AFM images of uncoated Si wafer and wafer coated with CP55 or CP55-60.

Water contact angle (CA) was also measured on the treated films to characterize their macroscopic hydrophilicity, which reflected the rate of conversion of the derivatization step and was correlated with the potential enthalpic penalty for foulant adhesion and thereby antifouling performance (Fig. 2A). The CA of PVI and PDVB were 16.9° ± 1.2° and 87.3° ± 0.3°, respectively. After copolymerization of the two components, CP55 presented a CA of 55.3° ± 2.3°, and due to the high DVB content in CP26 and CP17, their CA values were 79.5° ± 0.5° and 78.9° ± 0.9°, respectively, approaching the CA of PDVB (Fig. 2A). The static CA images obtained during those measurements were included in fig. S6. The films treated with the vapor of 1,3-propanesultone demonstrated greatly reduced water CA values. With the increasing derivatization temperatures, the CA generally decreased for all three precursor polymers. Among these surfaces, CP55-60 and CP55-100 exhibited superhydrophilic properties (i.e., CA values below 10°), with the CA values of 9.9° ± 2.1° and 7.5° ± 0.7° for CP55-60 and CP55-100, respectively, despite having a DVB content of as high as 45%. That superhydrophilicity was attributed to the surface-concentrated zwitterionic moiety, demonstrated using high-resolution XPS. The diffusion-limited derivatization spontaneously created a concentration gradient from the coating surface to the bulk film, with the highest conversion achieved at the topmost surface, demonstrated by the depth profiling of imidazolium and imidazole contents (fig. S7) (*41*).

We further demonstrated that the iCVD coatings reserved the morphology of the underlying substrates, i.e., the surface roughness captured using atomic force microscope (AFM) remained unchanged before and after the iCVD process and the derivatization (Fig. 2C). Compared to the surface roughness of uncoated Si wafers [0.11 ± 0.01 nm root mean square (RMS) roughness], the Si wafers were coated with CP55, and CP55-60 exhibited RMS roughness values of 0.51 ± 0.06 and 0.44 ± 0.08 nm, respectively. The exceptional smoothness also ensured minimum exposure of available binding sites for virus or bacteria to attach.

Deactivation of human coronavirus HCoV-OC43 via contacting the imidazolium-based zwitterionic polymer

The antiviral activities of the imidazole-based zwitterionic polymer were measured using HCoV-OC43, a human *Betacoronavirus* that belongs to the same genus as SARS-CoV-2 but with lower lethality (*42*). This choice was made to ensure applicability of the results reported here to the pandemic-causing pathogen while minimizing the risk of the experiments described below. To benchmark

the antiviral activities, we compared the repulsion and deactivation efficacies of imidazolium-based zwitterionic polymers against those of glass, PVC, and Cu, representing a range of inorganic, plastic, and metal surfaces commonly used in public, health care, and manufacturing facilities. The antiviral activities of those surfaces were characterized using two approaches to capture (i) deactivation of viruses under dry ambient conditions, as discussed below, and (ii) repulsion of viruses under submerged aqueous conditions, which is discussed in the next section.

Virus deactivation was assessed using a process that we developed to mimic the drying of virus-containing fluids on a surface under dry ambient conditions. A suspension of the HCoV-OC43 virus [10 μl, cultured by following an established protocol using HCT-8 as the host cell (*43*)] was applied onto the aforementioned surfaces [i.e., glass, PVC, Cu, and the coating CP55-60 (applied on glass slides)], which were allowed to air dry at laboratory ambience for around 30 min. Once no visible liquid was confirmed, the surfaces were subsequently incubated at 34°C under 50% relative humidity for 24 hours, by the end of which, viruses were collected via vigorous washing by phosphate-buffered saline (PBS) and assessed for their infectivity. The HCT-8 cells were used again as host cells in the infectivity assay. The HCoV-OC43 suspended in PBS solution was inoculated to HCT-8 cells at a multiplicity of infection (MOI) of 0.05, and then, the virus culture was quantified at 36 hours after infection. Subsequently, the HCT-8 and HCoV-OC43 were stained by Hoechst 33358 and primary anti–HCoV-OC43 S antibodies and Alexa Fluor 568–labeled goat anti-rabbit immunoglobulin G (IgG), respectively, for imaging.

As shown in Fig. 3A, different colors were applied to distinguish between HCT-8 and HCoV-OC43, where the nuclei are shown in blue and the stained virus is shown in red. The presence of a large number of virus particles around a particular cell nucleus, shown as a bright red area around the blue area, indicates that the cell is infected while the virus is proliferating in the cell. Such cell is marked as infected cell. The infectivity of the inoculated virus can be indirectly known by the statistics of the percentage cell infected by the virus.

As shown in Fig. 3B, the lowest infectivity (i.e., the ratio of the infected cells to the total cells) of 13.4% was achieved for CP55-60 surfaces among the four surfaces, whereas, under the same conditions, viruses on glass, PVC, and Cu surfaces presented infectivity of 28.0, 31.5, and 51.5%, respectively. That capability of CP55-60 to deactivate coronaviruses under dry ambient conditions was attributed to a variety of molecular interactions between the imidazolium-based zwitterionic polymer and aromatic-rich amino acids through cation-π interactions or polar interactions, leading to denaturation of proteins (i.e., the spike glycoprotein lining the surface of SARS-CoV-2) upon contacting zwitterionic moieties. Such interaction is theoretically stronger for imidazolium-based zwitterionic polymer because the carbon atom at the C2 position of imidazolium carries a considerable positive charge. Such charge makes its hydrogen an excellent hydrogen-bond donor, enabling enhanced interactions with amino acids.

Reduced adhesion of human coronavirus HCoV-OC43 on the imidazolium-based zwitterionic polymer

Repulsion of viruses under submerged aqueous conditions was also quantified to assess the ability of the imidazolium-based zwitterionic polymer to resist the adhesion of viruses under physiologically relevant conditions. The aforementioned surfaces were incubated with HCoV-OC43 virus suspensions, with the median tissue culture infectious dose ($TCID_{50}$, a measure of viral titer) of $10^{7.5}$/ml, which was stock solution with the highest concentration, at room temperature for 30 min for virus to adhere. Virus attached to surface via physical adsorption and exhibited little correlation with the incubation time (*44*). Therefore, we chose a relatively short incubation time to capture the potential adhesion of virus.

The adhesion density of the virus particles was characterized using scanning electron microscope (SEM) images (Fig. 3C). To ensure the statistical representativeness of our results, we took four nonoverlapping SEM images on each surface with a field of vision that is 25 μm by 15 μm (see detailed data analysis in fig. S8 and the Supplementary Materials). That size of the field of vision was chosen to be large enough to capture a statistical average of the virus adhesion without losing the resolution required to correctly identify the virus nanoparticles, which were merely 100 to 200 nm on average and with a spherical shape (fig. S9).

As shown in Fig. 3C, CP55-60 exhibited the lowest amount of virus adhesion at the end of the incubation period among all surfaces tested. Compared to the virus adhesion densities on control group surfaces, which were calculated to be $8.1 \times 10^6/cm^2$ (glass), $1.4 \times 10^6/cm^2$ (PVC), and $4.3 \times 10^5/cm^2$ (Cu), the adhesion density was reduced by 97.4% on the surface coated with CP55-60 to $2.1 \times 10^5/cm^2$ compared with the glass surface.

Previous research has indicated that zwitterionic polymers synthesized using the two-step vapor-based method can have a mild negative charge (e.g., ζ potential was around −13 mV for a pyridinium-based zwitterionic polymer in a 100 mM NaCl standard solution at the pH of 7) (*26*). Although negative surface charge is desirable because virus particles are also believed to be negatively charged (*45*), we do not anticipate electrostatic repulsion to be the primary reason for the reduction of viral adhesion, as charge neutrality is a prerequisite for the antibiofouling behavior demonstrated by the imidazolium zwitterionic polymers reported here. We believe such reduction in viral adhesion is attributed to strong hydration and charge-neutral nature of CP55-60, minimize the nonspecific binding between viral particles and surface (*15*, *46*).

Reduced biofilm formation and production of siderophores on the imidazolium-based zwitterionic polymer

In addition to the excellent antiviral performance, the imidazolium-based zwitterionic polymer also led to reduced biofilm formation, which was comparable to the antifouling performance of methacrylate- or pyridine-based zwitterionic polymers reported to date (*47*). To characterize the fouling resistance of CP55-60, *P. aeruginosa*, strain PAO1, was selected as the model organism for its known ability to rampantly produce biofilm (*48*) and the large amount of hospitalization cases caused by PAO1 each year (*49*).

Biofilm growth was quantified using the O'Toole protocol (*50*), which has been adapted to characterize antifouling performance of planar substrates and coated surfaces (*43*). The CP55-60 coating exhibited reduced biofilm formation compared to the PVC materials commonly used in health care facilities, where the amount of biofilm captured on the coated surface was 16% that of PVC, measured using the crystal violet staining approach (*50*). By comparison, nonderivatized CP55 or PDVB incurred biofilm growth that was comparable to PVC (Fig. 4A). Furthermore, the reduced biofilm formation on CP55-60 was not due to its antimicrobial effect, as the

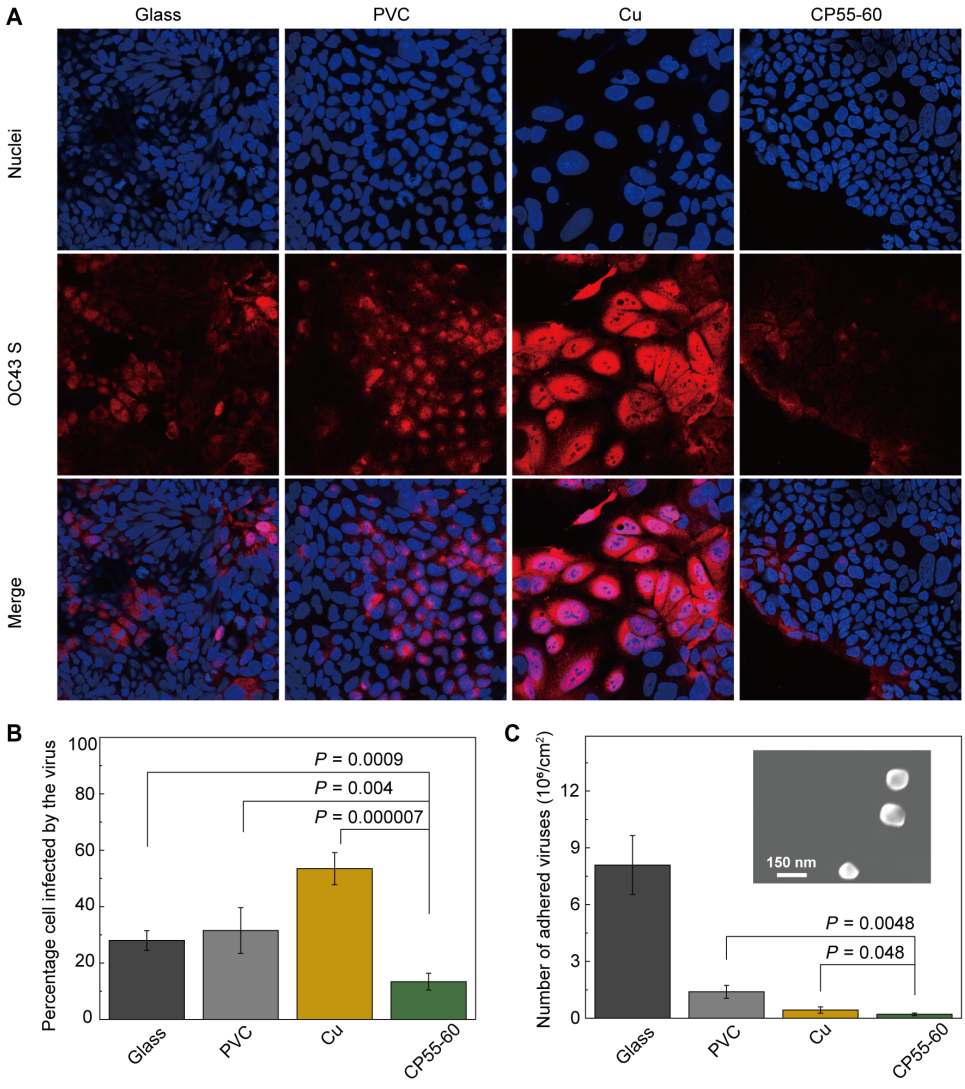

Fig. 3. Enhanced deactivation and repulsion of HCoV-OC43 on the imidazolium-based zwitterionic polymers. (**A**) Immunofluorescence imaging of the HCoV-OC43-infected HCT-8 cells taken at 36 hours after infection on glass, PVC, Cu, and the CP55-60 coating. MOI of 0.05; HCoV-OC43 S. The spike protein in HCoV-OC43 was marked as red using primary anti–HCoV-OC43 S antibodies and Alexa Fluor 568–labeled goat anti-rabbit IgG, and cell nuclei were marked as blue using Hoechst 33358. (**B**) Percentage of cells infected by HCoV-OC43 that settled on the four surfaces, calculated by analyzing Fig. 3A using ImageJ. Data are shown as the means ± SD ($n = 5$); P values were calculated using Student's t test. (**C**) Number of attached virus particles on glass, PVC, Cu, and CP55-60 surfaces counted from SEM images of each surface. Data are shown as the mean ± SD ($n = 4$); P values were calculated using Student's t test. The inset shows a representative SEM image of surface-attached HCoV-OC43.

liquid culture incubated with all surfaces demonstrated similar stationary optical density at 600 nm (OD_{600}) (fig. S10). It is worth nothing that the imidazolium-based zwitterionic coatings are distinct from extant antimicrobial coatings as bacteria were not deactivated on the zwitterionic surface. The strong hydration on zwitterionic surfaces suppresses adhesion of cells without the need for killing them. As a result, zwitterionic surfaces commonly have a much longer-lasting effect of inhibiting biofilm formation compared to antimicrobial surfaces (*51*). SEM images of the PAO1 biofilms grown on the four surfaces were captured to gain further insight into the effect of the surface chemistry on biofilm physiology (Fig. 4B). PVC, PDVB, and CP55 showed a thick biofilm with dense extracellular polymeric substances (EPS), whereas biofilm grown on the CP55-60 displayed sparse thread-like EPS.

The rampant PAO1 biofilm constantly secrets virulence factors, such as pyoverdine, removing substantial amounts of ferric ion from the host and causing severe toxicity to mammalian cells such as mitochondrial damage, reduced electron transfer and adenosine 5′-triphosphate production, and, ultimately, mitochondrial turnover (*52*). Inhibition of the production of microbial pyoverdine thus has the potential to mitigate the virulence from *P. aeruginosa* (*23*). To demonstrate that the imidazolium-based zwitterionic polymers was able to reduce the production of pyoverdine, the amount of pyoverdine in supernatant was measured by the fluorescent intensity at 460 nm and subsequently normalized by the OD_{600} to offset the potential variations in the culture conditions. Compared with CP55, PDVB, or PVC surface, CP55-60 significantly reduced the production of pyoverdine (Fig. 4C), which was attributed to the limited biofilm formation.

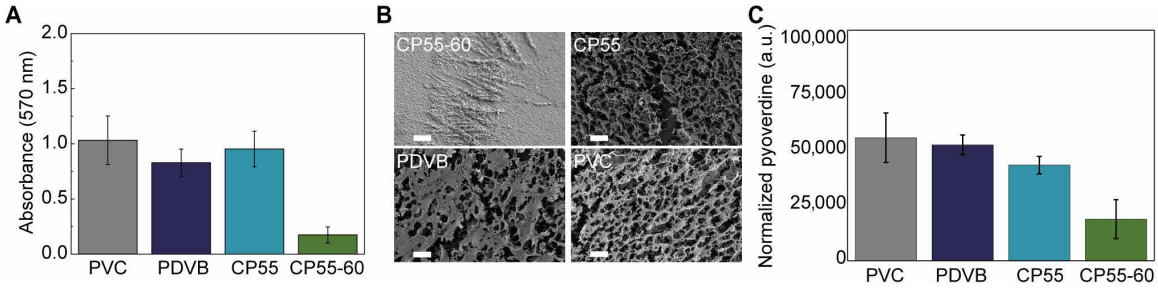

Fig. 4. Reduced biofilm formation and production of pyoverdine on the CP55-60 surfaces. (**A**) Absorbance measurements of the crystal violet staining and (**B**) SEM images of the biofilms after incubating for 24 hours with uncoated PVC and PVC coated with PDVB, underivatized CP55, and the CP55-60. Biofilms on CP55, PDVB, and PVC exhibited greater numbers of bacteria and thick and mature EPS structures, whereas the biofilms on CP55-60 grew to a less degree with sparse EPS. Scale bar, 20 microns. (**C**) Fluorescence measurements of the production of pyoverdine after a 24-hour incubation with uncoated PVC and those coated with PDVB, underivatized CP55, and the CP55-60. The fluorescence emission at 460 nm, representative of pyoverdine, was normalized by the OD_{600} of the culture medium. Data are shown as means ± SD ($n = 6$).

Substrate-independent and conformal nature of the solvent-free synthesis approach

The all-dry synthesis approach described above was used to create pyridinium-based zwitterionic coatings on substrates that are (i) curved with centimeter-level curvature (i.e., 96-well plates; Fig. 5A), (ii) microporous with convoluted 3D structures (i.e., glass fiber filters; Fig. 5B), and (iii) nanoporous with aspect ratios as high as 165 (i.e., polycarbonate membranes with 800-nm pores; Fig. 5C). The substrate morphology was well preserved with a 600-nm-thick coating on the 96-well plates, a 200-nm coating on glass fiber, and a 10-nm coating on polycarbonate membranes. The thickness for each coating is less than 10% of their characteristic length to maintain their original morphology.

Successful synthesis of the CP55-60 coatings on the variety of substrates and the coating conformality were proven using SEM energy dispersive x-ray analysis (EDX), where elemental mapping of sulfur, the element that was only present in the CP55-60 coating and not in any of the substrates, indicated the presence of the coating. Furthermore, the distribution of sulfur overlapped entirely with the underlying nano- and microstructures (Fig. 5, B and C) on the coated substrates, implying the excellent conformality of the CP55-60 coating. The conformality, combined with the substrate independence of this synthesis approach, pointed to the broad applications of the imidazolium-based zwitterionic polymer across a wide range of industries such as health care and manufacturing, and promised their reproducible synthesis and consistent antiviral and antifouling performance to mitigate public health threats.

DISCUSSION

We developed an imidazolium-based zwitterionic polymer that demonstrated effective contact deactivation and adhesion repelling of a human coronavirus, HCoV-OC43. The design of the imidazolium-based zwitterionic chemistry was based on the known antifouling properties of zwitterionic chemistries, as well as the interactions between zwitterionic moieties and aromatic amino acids, which are prevalent in the spike glycoprotein of coronaviruses, leading to potential virus deactivation.

To mimic the process of fomite transmission of coronaviruses, the effect of contact deactivation was demonstrated by applying HCoV-OC43–containing drops (representing aerosols) to the imidazolium-based zwitterionic polymer, a Cu surface, glass, and PVC, and letting the drops evaporate before quantifying the infectivity of the HCoV-OC43. That approach revealed that merely contacting the imidazolium-based zwitterionic polymer reduced infectivity of HCoV-OC43 to 13.4%, corresponding to a 74% reduction of infectivity compared to a Cu surface, which has been considered antimicrobial (*6*). Viruses deactivate naturally on a surface due to dehydration. The half-life of viruses on an untreated common surface has been reported to be 10 to 32 hours at 30°C (*1*), within which fomite transmissions present a severe threat to human health. On the CP55-60 surface, due to the hypothesized interaction between imidazolium and viruses, that deactivation was accelerated. Longer virus-surface contact time will likely cause further deactivation of the viruses due to the combined effect of the imidazolium chemistry and dehydration of virus particles.

The imidazolium-based zwitterionic polymer also demonstrated excellent antifouling properties under wetted conditions. Adhesion repelling was assessed by incubating the polymer with HCoV-OC43 suspensions, followed by quantification of the number of virus particles that adhered onto the surface. The imidazolium-based zwitterionic polymer showed a 97.4% reduction of the adhesion of viruses compared to a glass surface, which is widely used. The polymer further reduced the formation of PAO1 biofilms by 84% and production of pyoverdine, a virulence factor secreted by the biofilms, by 33%, compared to a standard PVC surface, proving fouling resistance while hinting at reduced virulence of the biofilms grown on the imidazolium-based zwitterionic polymers.

A substrate-independent and conformal synthesis approach was developed to enable the facile deployment of the zwitterionic coating reported here in a broad range of facilities. A variety of substrates, with curved surfaces and/or high-aspect-ratio nano/microporous structures, were successfully coated by the imidazolium-based zwitterionic polymers using the iCVD approach. Although the two-step synthesis procedure will likely increase the complexity of the process design during scale-up, both steps could be completed in a single vacuum chamber, thus improving its compatibility with industrial manufacturing configurations. The recent breakthroughs in achieving roll-to-roll manufacturing using iCVD (*53*, *54*) further supported the potential of the vacuum processes to be scaled up, where conformal and uniform coatings were obtained on flexible substrates as large as 20 m^2. Hence, the vacuum-based processing promises rapid deployment of the materials and the synthesis method reported here to protect public health and reduce the economic penalty associated with controlling fomite transmissions.

The imidazolium-based zwitterionic polymers exhibited excellent antiviral and antifouling performance. Although further increasing

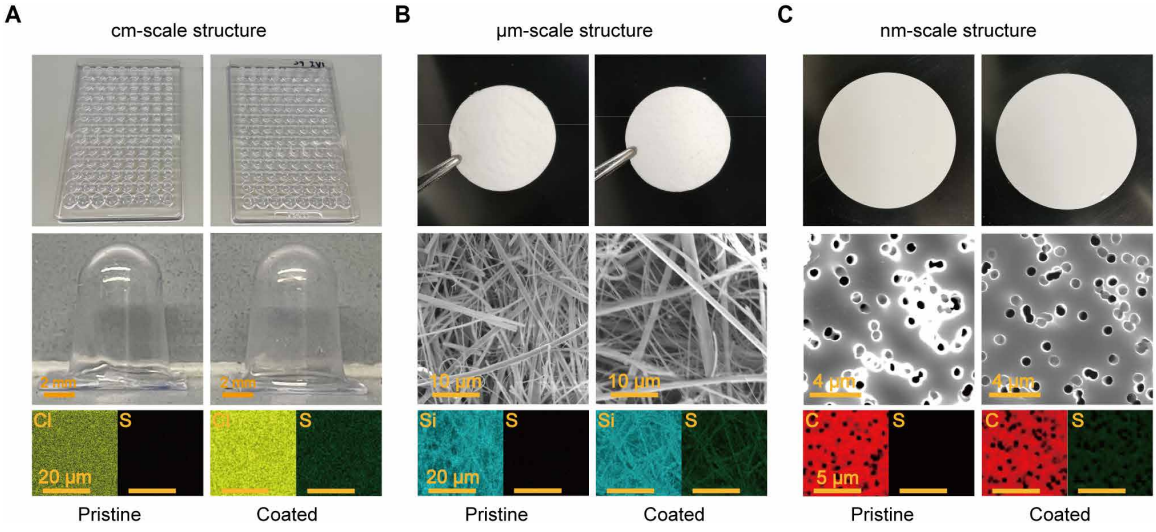

Fig. 5. Demonstration of the substrate-independent nature of the synthesis approach. (**A**) Optical images and elemental mapping obtained using SEM-EDX of pristine and coated 96-well plates, representing curved substrates. (**B**) Optical images, SEM images, and SEM-EDX elemental mapping of pristine and coated glass fiber filter with micrometer-level 3D structures. (**C**) Optical images, SEM images, and SEM-EDX elemental mapping of pristine and coated polycarbonate membrane filters with 800-nm pores.

the content of the imidazolium-based zwitterionic moieties, e.g., beyond the content of 55% that was achieved here, could enhance their antiviral efficacy, the low reactivity of VI (*55*) limited its incorporation into the copolymer. An important future research goal is to increase VI content via optimization of the cross-linker or replacing VI with other imidazolium-enabling monomers that are more reactive. Furthermore, despite the hypothesized C2-mediated antiviral mechanism and the demonstrated antiviral efficacy, the fundamental mechanism of virus deactivation on the imidazolium-based zwitterionic polymers remained elusive, which is a critical focus of our current and future research. In addition, although film thickness is unlikely to affect the antiviral/antifouling performance of CP55-60 due to its high degree of cross-linking and smooth morphology, the effect of thickness on the film long-term stability and performance remains an important focus of our future research. Nevertheless, the antiviral zwitterionic polymer represents a substantial advancement in the design of materials to combat coronaviruses. The substrate-independent application of the polymer as coatings hints at a broad and facile deployment, which will reduce the economic and health impact of the COVID-19 pandemic.

MATERIALS AND METHODS

Initiated chemical vapor deposition

All the polymeric coatings were created using the iCVD technology in a custom-built cylindrical vacuum reactor (Sharon Vacuum Co Inc., Brockton, MA, USA). Thermal excitation of the initiators was provided by heating a 0.5-mm nickel/chromium filament (80% Ni/20% Cr, Goodfellow) mounted as a parallel filament array. Filament temperature was controlled by a feedback loop, whose reading came from a thermocouple attached to one of the filaments. The filament holder straddled the deposition stage that was kept at desired substrate temperatures using a chiller. The vertical distance between the filament array and the stage was ~2 cm. Depositions were performed on various substrates: Si wafers (P/Boron <100>, Purewafer), 96-well microplates (2797, Corning), glass slides (Thermo Fisher Scientific), petri dish (Thermo Fisher Scientific), copper foil (MTI Corporation), PVC sheets (McMaster-Carr), and glass fiber filter and polycarbonate membrane filters (Sigma-Aldrich). Cooling of the microplates was further enhanced by a custom-designed aluminum holder. Initiator [*tert*-butyl peroxide (TBPO) (98%; Sigma-Aldrich)] and monomers [VI (99%; Sigma-Aldrich) and DVB (Sigma-Aldrich, 80%)] were used without further purification. During the iCVD depositions, TBPO and argon patch flow were fed to the reactor at room temperature through mass flow controllers at 1.0 standard cubic centimeter per minute and desired flow rates, respectively. VI was heated to 70°C in glass a jar to create sufficient pressure to drive vapor flow. Films were deposited at a filament temperature of 230°C. The total pressure of the chamber was controlled by a butterfly valve. In situ interferometry with a HeNe laser source (wavelength = 633 nm, JDS Uniphase) was used to monitor the film growth on a Si substrate.

Derivatization

The coated substrates were fixed in a crystallizing dish (VWR) with 1 g of 1,3-propanesultone (98%; Sigma-Aldrich). The crystallizing dish was placed inside a vacuum oven that was maintained at desired temperature for 24 hours to allow the 1,3-propanesultone vapor to react with the PVI-*co*-DVB coating.

Polymer film characterization

FTIR measurements were performed on a Bruker Vertex V80v vacuum FTIR system in transmission mode. A deuterated triglycine sulfate KBr detector over the range of 400 to 4000 cm^{-1} was adopted with a resolution of 4 cm^{-1}. The measurements were averaged more than 64 scans to obtain a sufficient signal-to-noise ratio. All the spectra were baseline-corrected by subtracting a background spectrum of Si.

During XPS, samples were analyzed using a Surface Science Instruments SSX-100 ESCA spectrometer with operating pressure ca. 1×10^{-9} torr. Monochromatic Al Kα x-rays (1486.6 eV) with photoelectrons were collected from a 800-μm-diameter area. Photoelectrons were collected at a 55° emission angle with source to analyzer angle of 70°. A hemispherical analyzer determined electron

kinetic energy using a pass energy of 150 eV for wide/survey scans and 50 eV for high-resolution scans. A flood gun was used for charge neutralization of nonconductive samples. Data analysis was conducted by CasaXPS with Shirley as the background. All the samples were stored under vacuum at room temperature for a week before XPS analysis. For the depth profiling of the imidazolium versus imidazole contents, the thin films of CP55-60, deposited on a Si wafer cut into pieces, were etched using ion milling. The etching depths of 20, 40, 60, and 100 nm, respectively, were sampled using XPS survey scans. The contents of imidazolium and imidazole groups were calculated by analyzing the content of sulfur (atomic ratio). The content of unreacted imidazole was calculated as complementary to the content of imidazolium.

CA measurements were performed using a Rame-Hart model 500 goniometer equipped with an automated water dispenser. Static CA measurements were recorded using a 2 μl droplet dispensed upon silicon wafers coated with the polymer thin films.

Surface roughness and topography were measured using an Asylum Research MFP-3D-BIO AFM. Scans were recorded across 2.5 μm–by–2.5 μm regions at 1.0 Hz in tapping mode.

The SEM images and elemental maps were obtained using Zeiss Gemini 500 with an acceleration voltage of 10 kV. Gold was sputter-coated onto all samples before imaging. The optical images were obtained using an iPhone 12 Pro.

Characterization of the antiviral efficacy

HCT-8 colon epithelial cells [American Type Culture Collection (ATCC) CCL-244] and H-CoV-OC43 (ATCC VR1558) were provided by the G. Whittaker Laboratory. HCT-8 cells were maintained in Dulbecco's modified Eagle medium (DMEM) (Corning, USA) with 10% fetal bovine serum (FBS) (Gibco, USA) and 1% penicillin/streptomycin (Gibco, USA). The cells were grown as monolayers at 37°C with 5% CO_2. H-CoV-OC43 was grown and propagated in HCT-8 cells at 34°C with 5% CO_2 in DMEM with 2% FBS and 1% penicillin/streptomycin. Infected cells were lysed 8 days after infection by two freeze-thaw cycles. The virus-containing fluid was cleared by centrifugation, aliquoted, and stored at −80°C. The titer of virus was $10^{7.5}$ $TCID_{50}$/ml.

The substrates (glass slide, Cu foil, PVC sheet, and glass slide coated with 600-nm CP55-60) were first cut into 1 cm–by–1 cm pieces. To make the virus attach to the surface, substrates were submerged into the virus suspension and were cultured for 30 min under room temperature. The substrates were then gently washed using 50, 70, 85, 95, and 100% ethanol in increasing concentration. The number of the attached viruses was counted from SEM images. The SEM images were obtained using Zeiss Gemini 500 with an acceleration voltage of 3 kV. A 2-nm gold layer was sputter-coated onto all samples before imaging.

To test surface inactivation, 10 μl of virus stock solution was dispersed on samples with a size of 1.5 cm by 1.5 cm. The sample was air-dried under room temperature before being transferred into an incubator maintained at 34°C and 50% humidity for 24 hours. The samples were then washed with a total amount of 1 ml of PBS repeatedly to transfer the virus to the solution. For the immunofluorescence assay, HCT-8 cells (5×10^4 cells per well) were cultured in 3.5-mm glass bottom dish (Cellvis, USA) and then infected with HCoV-OC43 at an MOI of 0.05 and cultured at 34°C for 36 hours. After 36 hours, HCT-8 cells were fixed with 4% paraformaldehyde. The fixed cells were washed twice with PBS and permeabilized with 0.5% Triton X-100 for 13 min at room temperature. Afterward, samples were blocked for 45 min at room temperature in 5% goat serum in PBS and incubated overnight at 4°C with primary anti–HCoV-OC43 S antibodies (Cusabio) diluted 1:500 in 3% goat serum in PBS. Subsequently, samples were incubated for 1 hour with Alexa Fluor 568–labeled goat anti-rabbit IgG (Thermo Fisher Scientific) diluted 1:1000 in PBS. Nuclei were stained with Hoechst 33258 (Thermo Fisher Scientific) diluted 1:10,000 in PBS. After immunostaining, in all the cases, the cells were washed with 0.5% Tween-20 in PBS. Last, stained cultures were mounted onto glass slides in ProLong Diamond antifade medium (Thermo Fisher Scientific) and stored at 4°C.

The infectivity (%) was calculated by the equation below. For each sample, cells from five different fields were counted

$$\%\ \text{of infected cells} = \frac{\text{OC 43 positive cell number}}{\text{Total cell number (Hoechst)}} \times 100$$

Biofilm formation

PAO1 from −80°C frozen stocks were streaked on a trichostatin A plate. The plate was placed in an incubator (37°C) overnight until single colonies were formed. A single colony was picked and inoculated into lysogeny broth (LB) medium. The inoculated medium was incubated overnight at 37°C to stationary phase in a shaker (225 rpm). The overnight suspension was diluted 100 times in fresh LB medium and incubated at 37°C on a shaker (225 rpm) until the optical density reached 0.2. Bacterial suspension of 150 μl was then added into each well of the surface-modified 96-well microplate. The microplates were incubated (37°C) for 24 hours to make sure biofilms were mature. The liquid was then transferred into a new microplate. The relative pyoverdine concentration can be obtained by exposure of the culture to a 405-nm excitation light and recording the fluorescence intensity at 460 nm. The rest of the liquid culture and loosely attached bacteria were removed from each well by vigorously washing each well three to four times with deionized water (dH_2O). Biofilms were then stained by 175 μl of dH_2O with 0.1 weight % crystal violet for 10 min. Then, the crystal violet solution was removed by washing each well three to four times until the liquid in each well became a clear solution. The microplate was dried in the air at room temperature for 24 hours to remove residual water in each well. The biofilm formed was subsequently quantified. A total of 200 μl of acetic acid solution (30 v/v%) was added into each well to release the absorbed crystal violet and the relative amount of absorbed crystal violet was quantified spectrophotometrically by measuring the OD_{570} using a microplate reader (Infinite M1000 Pro, Tecan).

To obtain SEM images of the biofilm, after incubating the microplates for 24 hours, the microplates with biofilm on the sidewall were treated with 0.05 M cacodylate buffer containing 2% glutaraldehyde and 1% osmium tetroxide for fixation. Samples were then dehydrated using critical point drying. The SEM images were obtained using Zeiss Gemini 500 with an acceleration voltage of 3 kV. Gold was sputter-coated onto all samples before imaging.

Statistical analysis

Experiments were carried out at least three times for statistical analysis. All data are expressed as means ± SD. Statistical significance was determined by paired Student's *t* test.

SUPPLEMENTARY MATERIALS

Supplementary material for this article is available at https://science.org/doi/10.1126/sciadv.abl8812

View/request a protocol for this paper from *Bio-protocol*.

REFERENCES AND NOTES

1. S. Riddell, S. Goldie, A. Hill, D. Eagles, T. W. Drew, The effect of temperature on persistence of SARS-CoV-2 on common surfaces. *Virol. J.* **17**, 145 (2020).
2. C. Xie, H. Zhao, K. Li, Z. Zhang, X. Lu, H. Peng, D. Wang, J. Chen, X. Zhang, D. Wu, Y. Gu, J. Yuan, L. Zhang, J. Lu, The evidence of indirect transmission of SARS-CoV-2 reported in Guangzhou, China. *BMC Public Health* **20**, 1202 (2020).
3. D. Lewis, COVID-19 rarely spreads through surfaces. So why are we still deep cleaning? *Nature* **590**, 26–28 (2021).
4. S. A. Kemp, D. A. Collier, R. P. Datir, I. A. T. M. Ferreira, S. Gayed, A. Jahun, M. Hosmillo, C. Rees-Spear, P. Mlcochova, I. U. Lumb, D. J. Roberts, A. Chandra, N. Temperton; The CITIID-NIHR BioResource COVID-19 Collaboration; The COVID-19 Genomics UK (COG-UK) Consortium, K. Sharrocks, E. Blane, Y. Modis, K. E. Leigh, J. A. G. Briggs, M. J. van Gils, K. G. C. Smith, J. R. Bradley, C. Smith, R. Doffinger, L. Ceron-Gutierrez, G. Barcenas-Morales, D. D. Pollock, R. A. Goldstein, A. Smielewska, J. P. Skittrall, T. Gouliouris, I. G. Goodfellow, E. Gkrania-Klotsas, C. J. R. Illingworth, L. E. McCoy, R. K. Gupta, SARS-CoV-2 evolution during treatment of chronic infection. *Nature* **592**, 277–282 (2021).
5. E. Goldman, Exaggerated risk of transmission of COVID-19 by fomites. *Lancet Infect. Dis.* **20**, 892–893 (2020).
6. S. M. Imani, L. Ladouceur, T. Marshall, R. Maclachlan, L. Soleymani, T. F. Didar, Antimicrobial nanomaterials and coatings: Current mechanisms and future perspectives to control the spread of viruses including SARS-CoV-2. *ACS Nano* **14**, 12341–12369 (2020).
7. J. O. Noyce, H. Michels, C. W. Keevil, Inactivation of influenza A virus on copper versus stainless steel surfaces. *Appl. Environ. Microbiol.* **73**, 2748–2750 (2007).
8. H. H. Lara, N. V. Ayala-Nuñez, L. Ixtepan-Turrent, C. Rodriguez-Padilla, Mode of antiviral action of silver nanoparticles against HIV-1. *J. Nanobiotechnol.* **8**, 1 (2010).
9. R. Nakano, M. Hara, H. Ishiguro, Y. Yao, T. Ochiai, K. Nakata, T. Murakami, J. Kajioka, K. Sunada, K. Hashimoto, A. Fujishima, Y. Kubota, Broad spectrum microbicidal activity of photocatalysis by TiO2. *Catalysts* **3**, 310–323 (2013).
10. F. Gelman, K. Lewis, A. M. Klibanov, Drastically lowering the titer of waterborne bacteriophage PRD1 by exposure to immobilized hydrophobic polycations. *Biotechnol. Lett.* **26**, 1695–1700 (2004).
11. A. M. Larson, B. B. Hsu, D. Rautaray, J. Haldar, J. Chen, A. M. Klibanov, Hydrophobic polycationic coatings disinfect poliovirus and rotavirus solutions. *Biotechnol. Bioeng.* **108**, 720–723 (2011).
12. Y. Si, Z. Zhang, W. Wu, Q. Fu, K. Huang, N. Nitin, B. Ding, G. Sun, Daylight-driven rechargeable antibacterial and antiviral nanofibrous membranes for bioprotective applications. *Sci. Adv.* **4**, eaar5931 (2018).
13. J. Kim, H. Lee, J.-Y. Lee, K.-H. Park, W. Kim, J. H. Lee, H.-J. Kang, S. W. Hong, H.-J. Park, S. Lee, J.-H. Lee, H.-D. Park, J. Y. Kim, Y. W. Jeong, J. Lee, Photosensitized production of singlet oxygen via C60 fullerene covalently attached to functionalized silica-coated stainless-steel mesh: Remote bacterial and viral inactivation. *Appl Catal B* **270**, 118862 (2020).
14. B. Alosaimi, A. Naeem, M. E. Hamed, H. S. Alkadi, T. Alanazi, S. S. Al Rehily, A. Z. Almutairi, A. Zafar, Influenza co-infection associated with severity and mortality in COVID-19 patients. *Virol. J.* **18**, 127 (2021).
15. J. B. Schlenoff, Zwitteration: Coating surfaces with zwitterionic functionality to reduce nonspecific adsorption. *Langmuir* **30**, 9625–9636 (2014).
16. R. Zhang, Y. Liu, M. He, Y. Su, X. Zhao, M. Elimelech, Z. Jiang, Antifouling membranes for sustainable water purification: Strategies and mechanisms. *Chem. Soc. Rev.* **45**, 5888–5924 (2016).
17. A. Wu, Y. Gao, L. Zheng, Zwitterionic amphiphiles: Their aggregation behavior and applications. *Green Chem.* **21**, 4290–4312 (2019).
18. A. A. Rodríguez-Sanz, E. M. Cabaleiro-Lago, J. Rodríguez-Otero, On the interaction between the imidazolium cation and aromatic amino acids. A computational study. *Org. Biomol. Chem.* **13**, 7961–7972 (2015).
19. A. Acharyya, D. Shin, T. Troxler, F. Gai, Can glycine betaine denature proteins? *Phys. Chem. Chem. Phys.* **22**, 7794–7802 (2020).
20. M. W. Howard, E. A. Travanty, S. A. Jeffers, M. K. Smith, S. T. Wennier, L. B. Thackray, K. V. Holmes, Aromatic amino acids in the juxtamembrane domain of severe acute respiratory syndrome coronavirus spike glycoprotein are important for receptor-dependent virus entry and cell-cell fusion. *J. Virol.* **82**, 2883–2894 (2008).
21. B. Li, P. Jain, J. Ma, J. K. Smith, Z. Yuan, H.-C. Hung, Y. He, X. Lin, K. Wu, J. Pfaendtner, S. Jiang, Trimethylamine *N*-oxide–derived zwitterionic polymers: A new class of ultralow fouling bioinspired materials. *Sci. Adv.* **5**, eaaw9562 (2019).
22. C. Jiang, G. Wang, R. Hein, N. Liu, X. Luo, J. J. Davis, Antifouling strategies for selective in vitro and in vivo sensing. *Chem. Rev.* **120**, 3852–3889 (2020).
23. D. Kang, A. V. Revtovich, Q. Chen, K. N. Shah, C. L. Cannon, N. V. Kirienko, Pyoverdine-dependent virulence of *Pseudomonas aeruginosa* isolates from cystic fibrosis patients. *Front. Microbiol.* **10**, 2048–2048 (2019).
24. Y. Cheng, A. Khlyustova, P. Chen, R. Yang, Kinetics of all-dry free radical polymerization under nanoconfinement. *Macromolecules* **53**, 10699–10710 (2020).
25. K. K. Gleason, Nanoscale control by chemically vapour-deposited polymers. *Nat. Rev. Phys.* **2**, 347–364 (2020).
26. P. Chen, J. Lang, T. Donadt, Z. Yu, R. Yang, Reduced biofilm formation at the air-liquid-solid interface via introduction of surfactants. *ACS Biomater Sci. Eng.* 10.1021/acsbiomaterials.0c01691, (2021).
27. R. Yang, K. K. Gleason, Ultrathin antifouling coatings with stable surface zwitterionic functionality by initiated chemical vapor deposition (iCVD). *Langmuir* **28**, 12266–12274 (2012).
28. Y. Yoo, B. G. Kim, K. Pak, S. J. Han, H.-S. Song, J. W. Choi, S. G. Im, Initiated chemical vapor deposition (iCVD) of highly cross-linked polymer films for advanced lithium-ion battery separators. *ACS Appl. Mater. Interfaces* **7**, 18849–18855 (2015).
29. J. Pavlinec, M. Lazár, I. Janigová, Influence of crosslinking on surface hardness of poly(methyl methacrylate). *J. Macromol. Sci. A* **34**, 81–90 (1997).
30. K. K. S. Lau, K. K. Gleason, Initiated chemical vapor deposition (iCVD) of poly(alkyl acrylates): An experimental study. *Macromolecules* **39**, 3688–3694 (2006).
31. D. Soto, A. Ugur, T. A. Farnham, K. K. Gleason, K. K. Varanasi, Short-fluorinated iCVD coatings for nonwetting fabrics. *Adv. Funct. Mater.* **28**, 1707355 (2018).
32. G. Ozaydin-Ince, K. K. Gleason, Transition between kinetic and mass transfer regimes in the initiated chemical vapor deposition from ethylene glycol diacrylate. *J. Vac. Sci. Technol. A* **27**, 1135–1143 (2009).
33. H. Chi, P. Chen, L. Cao, X. Wu, J. Wang, Characterization and adsorptive properties of cross-linked poly (1-vinylimidazole)-iron (III) complex synthesized in supercritical carbon dioxide. *e-Polymers* **16**, 403–410 (2016).
34. D. Lin-Vien, N. B. Colthup, W. G. Fateley, J. G. Grasselli, Chapter 1 - Introduction, in *The Handbook of Infrared and Raman Characteristic Frequencies of Organic Molecules*, D. Lin-Vien, N. B. Colthup, W. G. Fateley, J. G. Grasselli, Eds. (Academic Press, 1991), pp. 1–7.
35. C. D. Petruczok, R. Yang, K. K. Gleason, Controllable cross-linking of vapor-deposited polymer thin films and impact on material properties. *Macromolecules* **46**, 1832–1840 (2013).
36. M. C. Burrell, M. D. Butts, D. Derr, S. Genovese, R. J. Perry, Angle-dependent XPS study of functional group orientation for aminosilicone polymers adsorbed onto cellulose surfaces. *Appl. Surf. Sci.* **227**, 1–6 (2004).
37. V. R. Sastri, Chapter 6 - Commodity thermoplastics: Polyvinyl chloride, polyolefins, and polystyrene, in *Plastics in Medical Devices*, V. R. Sastri, Ed. (William Andrew Publishing, 2010), pp. 73–119.
38. R. Yang, H. Jang, R. Stocker, K. K. Gleason, Synergistic prevention of biofouling in seawater desalination by zwitterionic surfaces and low-level chlorination. *Adv. Mater.* **26**, 1711–1718 (2014).
39. A. G. Kuba, Y. Y. Smolin, M. Soroush, K. K. S. Lau, Synthesis and integration of poly(1-vinylimidazole) polymer electrolyte in dye sensitized solar cells by initiated chemical vapor deposition. *Chem. Eng. Sci.* **154**, 136–142 (2016).
40. S. Bag, A. Samanta, P. Bhunia, C. R. Raj, Rational functionalization of reduced graphene oxide with imidazolium-based ionic liquid for supercapacitor application. *Int. J. Hydrogen Energy* **41**, 22134–22143 (2016).
41. T. B. Donadt, R. Yang, Amphiphilic polymer thin films with enhanced resistance to biofilm formation at the solid-liquid-air interface. *Adv. Mater. Interfaces* **8**, 2001791 (2021).
42. B. Chen, E.-K. Tian, B. He, L. Tian, R. Han, S. Wang, Q. Xiang, S. Zhang, T. El Arnaout, W. Cheng, Overview of lethal human coronaviruses. *Signal Transduct. Target. Ther.* **5**, 89 (2020).
43. K. Owczarek, A. Szczepanski, A. Milewska, Z. Baster, Z. Rajfur, M. Sarna, K. Pyrc, Early events during human coronavirus OC43 entry to the cell. *Sci. Rep.* **8**, 7124–7124 (2018).
44. I. Kukavica-Ibrulj, A. Darveau, J. Jean, I. Fliss, Hepatitis A virus attachment to agri-food surfaces using immunological, virological and thermodynamic assays. *J. Appl. Microbiol.* **97**, 923–934 (2004).
45. M. V. Arkhipenko, N. A. Nikitin, O. A. Baranov, E. A. Evtushenko, J. G. Atabekov, O. V. Karpova, Surface charge mapping on virions and virus-like particles of helical plant viruses. *Acta Naturae* **11**, 73–78 (2019).
46. B. Li, Z. Yuan, P. Jain, H.-C. Hung, Y. He, X. Lin, P. McMullen, S. Jiang, De novo design of functional zwitterionic biomimetic material for immunomodulation. *Sci. Adv.* **6**, eaba0754 (2020).
47. T. B. Donadt, R. Yang, Vapor-deposited biointerfaces and bacteria: An evolving conversation. *ACS Biomater Sci. Eng.* **6**, 182–197 (2020).
48. C. K. Stover, X. Q. Pham, A. L. Erwin, S. D. Mizoguchi, P. Warrener, M. J. Hickey, F. S. L. Brinkman, W. O. Hufnagle, D. J. Kowalik, M. Lagrou, R. L. Garber, L. Goltry, E. Tolentino, S. Westbrock-Wadman, Y. Yuan, L. L. Brody, S. N. Coulter, K. R. Folger, A. Kas, K. Larbig, R. Lim, K. Smith, D. Spencer, G. K. S. Wong, Z. Wu, I. T. Paulsen, J. Reizer, M. H. Saier, R. E. W. Hancock, S. Lory, M. V. Olson, Complete genome sequence of *Pseudomonas aeruginosa* PAO1, an opportunistic pathogen. *Nature* **406**, 959–964 (2000).

49. Antibiotic resistance threats in the United States (2019); https://www.cdc.gov/drugresistance/pdf/threats-report/2019-ar-threats-report-508.pdf.
50. G. A. O'Toole, Microtiter dish biofilm formation assay. *J. Vis. Exp.*, 2437 (2011).
51. G. Cheng, Z. Zhang, S. Chen, J. D. Bryers, S. Jiang, Inhibition of bacterial adhesion and biofilm formation on zwitterionic surfaces. *Biomaterials* **28**, 4192–4199 (2007).
52. D. Kang, D. R. Kirienko, P. Webster, A. L. Fisher, N. V. Kirienko, Pyoverdine, a siderophore from *Pseudomonas aeruginosa*, translocates into *C. elegans*, removes iron, and activates a distinct host response. *Virulence* **9**, 804–817 (2018).
53. H. Şakalak, K. Yılmaz, M. Gürsoy, M. Karaman, Roll-to roll initiated chemical vapor deposition of super hydrophobic thin films on large-scale flexible substrates. *Chem. Eng. Sci.* **215**, 115466 (2020).
54. C. Cheng, M. Gupta, Roll-to-roll surface modification of cellulose paper via initiated chemical vapor deposition. *Ind. Eng. Chem. Res.* **57**, 11675–11680 (2018).
55. K. L. Petrak, Reactivity of some vinylimidazoles towards other vinyl monomers in radical copolymerization. *J. Polym. Sci. A Polym. Chem.* **16**, 393–399 (1978).

Acknowledgments: We thank G. Whittaker for discussions on experimental design and techniques regarding virus culture, quantification, and infectivity assays. **Funding:** We acknowledge the NIH–National Institute on Deafness and Other Communication Disorders for support (NIHDC016644 to R.Y.). Furthermore, the project is sponsored by the Department of the Navy, Office of Naval Research under ONR award N00014-20-1-2418. Analytical methods involved use of the Cornell Center for Materials Research (CCMR) Shared Facilities, which are supported through the NSF MRSEC program (DMR-1719875). **Author contributions:** R.Y., P.C., J.L., Y.Z., X.M., S.L., and Y.C. designed the research and conducted the experiments. A.K. provided graphic design for Fig. 1. R.Y., P.C., and Z.Z. performed the data analysis. P.C. and R.Y. drafted the manuscript. All authors provided critical feedback on experimental design and data analysis and reviewed the manuscript. **Competing interests:** P.C. and R.Y. are authors on a patent application filed by Cornell University (no. 63/263,999, filed 12 November 2021.) The authors declare that they have no other competing interests. **Data and materials availability:** All data needed to evaluate the conclusions in the paper are present in the paper and/or the Supplementary Materials.

Submitted 17 August 2021
Accepted 22 November 2021
Published 14 January 2022
10.1126/sciadv.abl8812